 doi:10.20944/preprints202107.0081.v1

Article

STUDY OF THE INFLUENCE OF A NONLINEAR CONTROL ALLOCATION FREQUENCY VARIATION ON A QUADROTOR TILT-ROTOR AIRCRAFT STABILITY

Murillo F. Santos[1], Paolo Mercorelli[2], Leonardo M. Honório[3], Mathaus F. Silva[3], Vinícius F. Vidal[3]

[1] Affiliation 1: Department of Electroelectronics, CEFET-MG, Leopoldina, Brazil
[2] Affiliation 2: Institute of Product and Process Innovation, Leuphana University, Lüneburg, Germany
[3] Affiliation 3: Faculty of Engineering, UFJF, Juiz de Fora, Brazil
* Correspondence: mercorelli@uni.leuphana.de
† Current address: Affiliation 2
‡ These authors contributed equally to this work.

Abstract: This paper presents a study on the influence of the frequency variation of a nonlinear control allocation technique execution, developed by the author [1], named by Fast Control Allocation (FCA) for the Quadrotor Tilt-Rotor (QTR) aircraft. Then, through Software In The Loop (SITL) simulation, the proposed work considers the use of Gazebo, QGroundControl, and Matlab applications, where different frequencies of the FCA can be implemented separated in Matlab, always analyzing the QTR stability conditions from the virtual environment performed in Gazebo. The results showed that the FCA needs at least 200 Hz of frequency for the QTR safe flight conditions, i. e., 2 times smaller than the main control loop frequency, 400 Hz. Lower frequencies than this one would case instability or crashes during the QTR operation.

Keywords: Over-Actuated Unmanned Aerial Vehicle; Nonlinear Control Allocation; Software In The Loop; Threshold Time.

1. Introduction

The applications of Unmanned Aerial Vehicles (UAVs) to perform tasks previously developed by humans are increasing every day, performing from medical to military tasks [2–5]. Among all possible applications, their topologies became a very important part of the whole project and execution, which are classified as fixed-wings (planes for example) and rotary wings (helicopters for example). A quick search on internet shows some reliable and stable UAVs, such as multicopters [6,7] and fixed-wings [8,9], for example.

Aiming to include the fixed-wing and rotary-wing classifications at the same vehicle, the hybrid topologies have emerged. A classic example is the Tilt-Rotors, which have tilting mechanisms for their propellers, making their maneuvers a partial combination of the two mentioned topologies. These tilt-rotors may or may not have fixed wings, just as many propellers may be required. These combinations let them being considered as overactuated vehicles, which are defined as UAV with more actuators than the respective Degrees of Freedom (DoF). Also, the overactuation directly interfere the system control allocation technique choice, which by definition is responsible for generating signals to the actuators from the control actions resulted from the controllers.

It is important to highlight that the vast majority of robotic systems do not require a complex method of control allocation, both for under and overactuated types. In addition, there are still cases where an overactuated UAV can be simplified as underactuated [10,11]. However, depending on the aircraft physical characteristics and design requirements, there is a strict necessity to use a non-linear and complex method [12].

 doi:10.20944/preprints202107.0081.v1

Recent researches reflect the existence of a wide variety of control allocation methodologies, already consolidated for linear models. For non-linear systems, there are numerous methodologies that depend specifically on the applied system [13]. Researches from literature remarks some interesting methods, which are: Direct Allocation; Pseudo-Inverse; Linear Programming; and Non-Linear Programming [10].

The Direct Allocation (DA) control technique considers the allocation space unconstrained with a specific pseudo-inverse, in a single iteration, satisfying only the control constraints. Consequently, it aims for a allocated parameters set that preserves the Virtual Control Actions (VCAs) direction [14]. The DA problem is not trivial for cases where the VCA size set is large [10].

Regarding Pseudo Inverse (PI) methods (such as by redistribution), the first step is to solve the problem without saturation constraints [15]. In the end, if the result satisfies the previously unrestricted actual control actions, no further steps are required. Otherwise, the optimal free vector with the Real Control Actions (RCAs) is designed in an appropriate configuration to reach the requirements [16].

In contrast to this methodology, Linear Programming (LP) minimizes the weighted error between the desired and estimated VCAs. Thus, an optimization problem with geometric / polyhedral constraints is represented. Using defined cost functions, the resulting problem is linearly programmable and can be solved using iterative numerical algorithms such as the simplex method [17].

Taking the Non Linear Programming (NLP) into consideration, there will always be a single optimal solution if all the weights in the cost function are necessarily positive using slack variables [18,19]. Referring to the numerical methods of solving, 3 algorithms deserve to be highlighted: active-set, interior point and fixed point methods.

However, an important point needs to be highlighted: as the solution complexity increases, the computational effort becomes a critical point when real-time execution is needed, due to the possibility of finding different local minima and numerical sensitivity in the evaluation and validation procedures. Also, the control allocation frequency evaluation becomes a crucial step in the whole UAV design, which means that if the RCAs are not obtained correctly, the system can become unstable and uncontrollable [12]. Aiming this aspect, it is possible to observe a large gap in the studies reporting these analysis, since incompatible control allocation technique frequencies can lead to instability on the vehicle, therefore generating accidents.

It is in this context that this work is proposed, presenting a study on the influence of the control allocation execution frequency variation for some simulation flight scenarios, being analyzed on the vehicle stability. Regarding the control allocation considered, it is used the nonlinear technique applied to the QTR developed in [1] and [12], illustrating a SITL representation.

The main contribution of this work is focused on establishing the minimum and safe frequency of the control allocation task, developed in work [1] and [12], where it was considered to be run in real-time and embedded execution at 400 Hz (same frequency as the QTR attitude control loop). Then, this work will study the minimum frequency able to still keep the QTR safely flying with the same control requirements previously set.

This paper is divided as follows: Section 2 presents the UAV kinemactics and dynamics modelling, strictly necessary for understanding the control allocation design and the simulation results; Section 3 depicts the considered controller topology, much as a brief overview of the Fast Control Allocation Technique proposed by [1,12]; Section 4 illustrates the SITL scheme to perform the results; Section 5 shows the simulation results, divided in kinematics and dynamics controlled results and the calculated time threshold values to run the control allocation technique without destabilizing the aircraft; Finally, Section 6 presents the conclusions of this work.

Preprints (www.preprints.org) | NOT PEER-REVIEWED | Posted: 5 July 2021 doi:10.20944/preprints202107.0081.v1

2. Non-Linear Aircraft Modelling and Control Allocation

Here is presented and depicted the aircraft kinematics and dynamics modelling, also considering the servomotor tilting angles. For better illustration, Fig. 1 shows the UAV and its axis rotations:

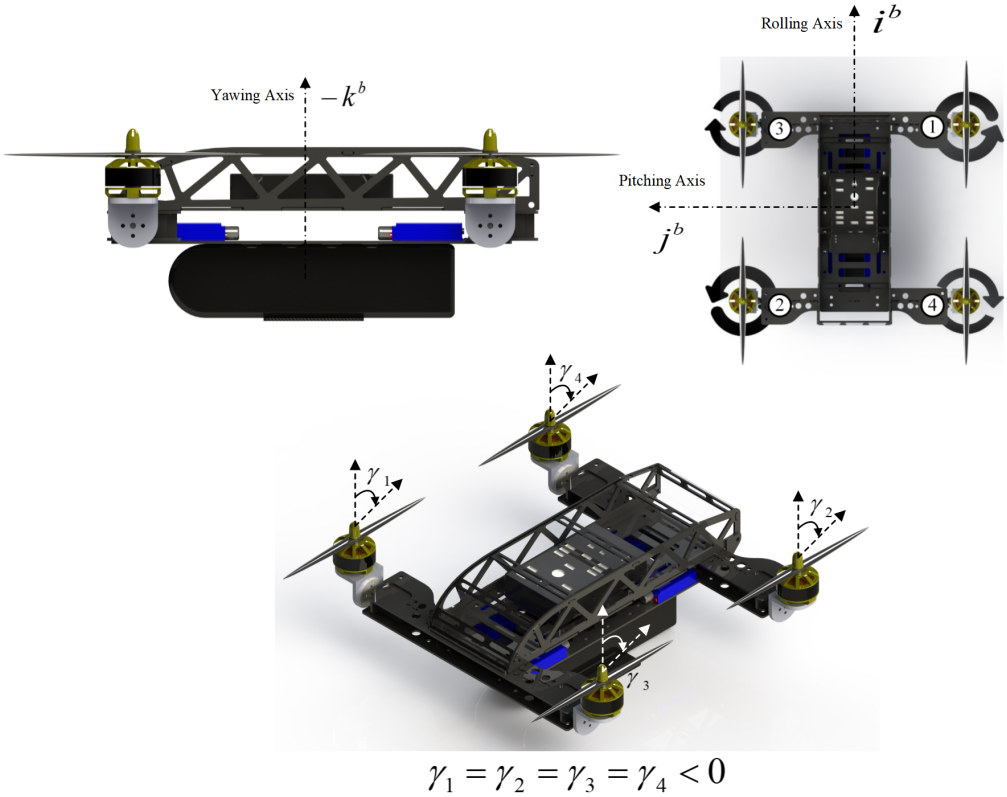

Figure 1. UAV illustration with respective rotation axes ($\gamma = 0$ degrees is the upward servomotor direction).

The numbers marked in the figure represent the propulsion motor and servomotor number, where 1 are in the front-right part of the QTR $\mathcal{F}^b$, number 2 are in the rear-left, number 3 are in the front-left and number 4 are in the rear-right. Furthermore, the propulsion motors 1 and 2 have counter-clockwise rotation, while 3 and 4 rotate clockwise. Also, the QTR RCAs $\boldsymbol{u} = [\delta_1, \delta_2, \delta_3, \delta_4, \gamma_1, \gamma_2, \gamma_3, \gamma_4]$ are the Propulsion Motors Speed (PMS) and tilting angles provided by all the motors and servomotors.

By consequence, considering that each set of motor propulsion force $k_i\delta_i$ and servomotor tilt angle γ_i has its own impact over the resultant virtual control variables [20]:

$$X^b_{p_i} = k_1\delta_i \sin(\gamma_i) \quad (1)$$

$$Z^b_{p_i} = k_1\delta_i \cos(\gamma_i) \quad (2)$$

$$L^b_{p_i} = (\pm k_1 d \cos(\gamma_i) \pm k_2 \sin(\gamma_i))\delta_i \quad (3)$$

$$M^b_{p_i} = k_1 d \cos(\gamma_i)\delta_i \quad (4)$$

$$N^b_{p_i} = (\pm k_1 d \sin(\gamma_i) \pm k_2 \cos(\gamma_i))\delta_i \quad (5)$$

where k_1 is the constant of propulsion, characteristic to each propulsion system (set of motor, electronic speed controller and propeller), k_2 is the constant of Newton's third law due to the propeller rotations, $d = 0.15m$ is the aircraft arm length, X^p_b and Z^p_b are

Preprints (www.preprints.org) | NOT PEER-REVIEWED | Posted: 5 July 2021 doi:10.20944/preprints202107.0081.v1

the forces produced by the propellers in $\mathcal{F}^b$ along axis $\hat{\boldsymbol{i}}^{\boldsymbol{b}}$ and $\hat{\boldsymbol{k}}^{\boldsymbol{b}}$, respectively, L_b^p, M_b^p and N_b^p are the torques produced by the propellers in $\mathcal{F}^b$ along axis $\hat{\boldsymbol{i}}^{\boldsymbol{b}}$, $\hat{\boldsymbol{j}}^{\boldsymbol{b}}$ and $\hat{\boldsymbol{k}}^{\boldsymbol{b}}$.

Then, the vehicle position is defined by the vector $\boldsymbol{\eta_1} \in \mathbb{R}^3$ in $\mathcal{F}^I$ (Inertial Frame), while its angles are defined by $\boldsymbol{\eta_2} \in \mathbb{R}^3$ in $\mathcal{F}^v$ (Vehicle Frame). Moreover, $\boldsymbol{\nu_1} \in \mathbb{R}^3$ and $\boldsymbol{\nu_2} \in \mathbb{R}^3$ are the linear and the angular velocities, measured in $\mathcal{F}^b$ (Body-Fixed Frame). According to [21], (7) presents the nomenclature:

$$\begin{aligned} \boldsymbol{\eta_1} &= [p_n \;\; p_e \; h]^T && (6)\\ \boldsymbol{\eta_2} &= [\phi \;\; \theta \;\; \psi]^T && (7)\\ \boldsymbol{\nu_1} &= [u \;\; v \;\; w]^T = [\boldsymbol{v^b}] && (8)\\ \boldsymbol{\nu_2} &= [p \;\; q \;\; r]^T = [\boldsymbol{\omega^b}] && (9) \end{aligned}$$

where $\boldsymbol{\eta} = [\boldsymbol{\eta_1} \;\; \boldsymbol{\eta_2}]^T$, $\boldsymbol{\nu} = [\boldsymbol{\nu_1} \;\; \boldsymbol{\nu_2}]^T$, $\boldsymbol{\nu_1} \in \mathbb{R}^3$ is the linear velocity vector, and $\boldsymbol{\nu_2} \in \mathbb{R}^3$ is the angular velocity vector, both in $\mathcal{F}^b$.

The 6 DoFs rigid body kinematics is expressed in (10):

$$\dot{\boldsymbol{\eta}} = \boldsymbol{J}\boldsymbol{\nu} \tag{10}$$

where $\dot{\boldsymbol{\eta}} \in \mathbb{R}^6$ is the velocity vector in $\mathcal{F}^I$, $\boldsymbol{\nu} \in \mathbb{R}^6$ is the general velocity vector in $\mathcal{F}^b$ and $\boldsymbol{J} \in \mathbb{R}^{6\times6}$ is the Jacobian matrix, where the position vector $\eta = \int \dot{\eta}$ is in $\mathcal{F}^I$.

The QTR dynamics can be described by differential equations from Newton-Euler method, such as shown in (11).

$$\boldsymbol{M^b}\dot{\boldsymbol{\nu}} + \boldsymbol{C^b}(\boldsymbol{\nu})\boldsymbol{\nu} = \boldsymbol{\tau_p^b} + \boldsymbol{\tau_a^b} + \boldsymbol{\tau_g^b} \tag{11}$$

where $\boldsymbol{M^b} \in \mathbb{R}^{6\times6}$ is the system inertia matrix, $\boldsymbol{C^b}(\boldsymbol{\nu}) \in \mathbb{R}^{6\times6}$ is the Coriolis-centripetal matrix, both in $\mathcal{F}^b$, and $\boldsymbol{\tau_a^b}$, $\boldsymbol{\tau_g^b}$, $\boldsymbol{\tau_p^b} \in \mathbb{R}^6$ are the Aerodynamics, Gravitational and Propulsion resultant vectors, respectively, composed of forces and torques, both in $\mathcal{F}^b$.

Equation (11) leads to highlight the definition of the Control Effectiness Matrix (CEM) represented by $\boldsymbol{\tau_p^b}$, which relates the effects of all the QTR actuator (RCAs) characteristics directly on the 5 controlled DoFs from the VCAs. Then, the actuator dynamics and their placements on the QTR is expressed in (13).

$$\boldsymbol{\tau_p^b} = \boldsymbol{M}(\boldsymbol{u}) \tag{12}$$

$$\begin{bmatrix} X_p^b \\ Z_p^b \\ L_p^b \\ M_p^b \\ N_p^b \end{bmatrix} = \begin{bmatrix} k_1\delta_1 s(\gamma_1) + k_1\delta_2 s(\gamma_2) + k_1\delta_3 s(\gamma_3) + k_1\delta_4 s(\gamma_4) \\ -k_1\delta_1 c(\gamma_1) - k_1\delta_2 c(\gamma_2) - k_1\delta_3 c(\gamma_3) - k_1\delta_4 c(\gamma_4) \\ (-k_1 dc(\gamma_1) - k_2 s(\gamma_1))\delta_1 + (k_1 dc(\gamma_2) - k_2 s(\gamma_2))\delta_2 + (k_1 dc(\gamma_3) + k_2 s(\gamma_3))\delta_3 + (-k_1 dc(\gamma_4) + k_2 s(\gamma_4))\delta_4 \\ +k_1 dc(\gamma_1)\delta_1 - k_1 dc(\gamma_2)\delta_2 + k_1 dc(\gamma_3)\delta_3 - k_1 dc(\gamma_4)\delta_4 \\ (-k_1 ds(\gamma_1) + k_2 c(\gamma_1))\delta_1 + (k_1 ds(\gamma_2) + k_2 c(\gamma_2))\delta_2 + (k_1 ds(\gamma_3) - k_2 c(\gamma_3))\delta_3 + (-k_1 ds(\gamma_4) - k_2 c(\gamma_4))\delta_4 \end{bmatrix} \tag{13}$$

where $\boldsymbol{\tau_p^b} \in \mathbb{R}^5$ is the estimated VCA vector, $\boldsymbol{u} \in \mathbb{R}^8$ is the RCAs vector inserted as parameters of the CEM $\boldsymbol{M} \in \mathbb{R}^5$, γ_i is the tilting angle of each servomotor (0 degrees has upward direction, $-\hat{\boldsymbol{k}}^{\boldsymbol{b}}$), δ_i is the rotation of each propulsion motor and i represents the respective servomotor and propulsion motor number. The propulsion force Y_p^b related to axis $\hat{\boldsymbol{j}}^{\boldsymbol{b}}$ is not represented because there is no direct force acting on this axis. After test bench experimental results, $k_1 = 7.0632$ and $k_2 = 0.1413$. For easy of representation, $c\gamma_i = \cos(\gamma_i)$ and $s\gamma_i = \sin(\gamma_i)$.

3. P-PID Controllers

It is known that UAV control systems are multiloops, that is, Multiple-Input-Multiple-Output (MIMO). In the vehicle in question, 5 DoFs are controlled, which are: altitude, forward/backward velocity, rolling, pitching and yawing movements. Four of them are composed of 2 cascade feedback loops excepts the forward/backward

Preprints (www.preprints.org) | NOT PEER-REVIEWED | Posted: 5 July 2021 doi:10.20944/preprints202107.0081.v1

velocity, which uses only 1 feedback loop. Also, all of them use the Successive Loop Closure (SLC) technique to deal with the iteration between the dynamics of altitude and with rolling, pitching and yawing.

To illustrate all the loops in a simplified form, Figure 2 shows the QTR overall control structure, where the control allocation task is marked with the circle number 3.

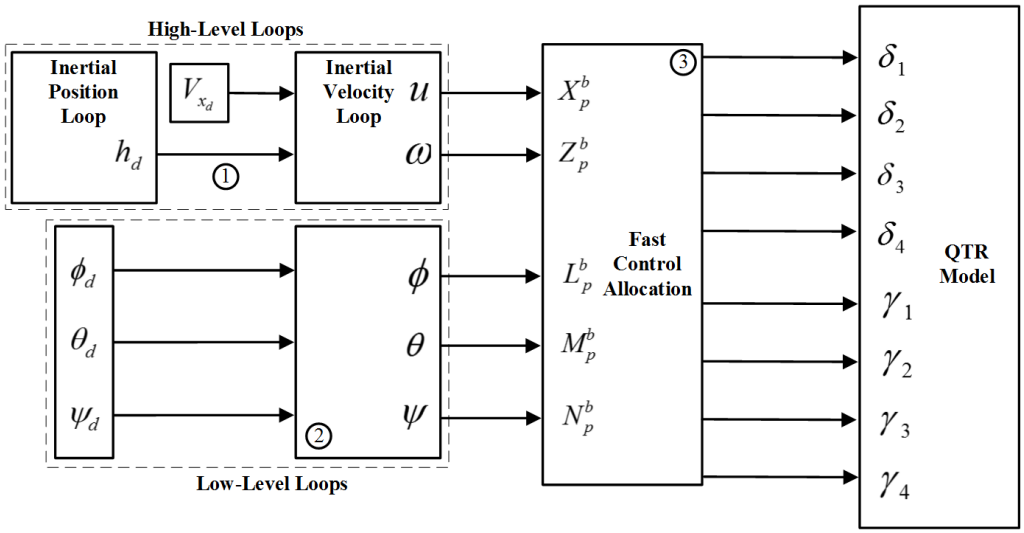

Figure 2. QTR overall control structure.

Considering each DoF with cascade loops, the external ones control the position variables through Proportional (P) controllers. The internal ones control their respective velocities, either inertial or angular, using Proportional-Integral-Derivative (PID) controllers. Thus, the control action output P will serve as input for the PID cascade internal controller [22].

A saturation block was also inserted in the integral loop, acting as an anti-windup action of the integrator. For the forward/backward velocity control loop (V_x), only 1 level was implemented through a PID controller.

Then, the MIMO closed control loop equation is presented in (14):

$$\left[\boldsymbol{\eta_d} - \left(\underbrace{\boldsymbol{M^b\dot{\nu} + C^b(\nu)\nu - \tau_a^b - \tau_g^b}}_{\text{from the QTR Model}}\right)\right]\boldsymbol{K^b} = \boldsymbol{\tau_p^b} \tag{14}$$

where $\boldsymbol{\eta_d} \in \mathbb{R}^5$ is the setpoint desired vector, and $\boldsymbol{K^b} \in \mathbb{R}^5$ are the actions from controller technique in $\mathcal{F}^b$.

More details about the QTR controllers and their tuning can be found in work [1].

3.1. The Fast Control Allocation Technique

As presented in (13), it is possible to see that the solution of the control allocation procedure has 5 VCAs (inputs) and 8 RCAs (outputs) with defined and non-unique solutions. Also, it is not possible to solve by matrix manipulation, instead more complex and time-consuming algorithms must be used (i. e., such as the primal-dual optimization algorithm [23]). These approaches make the processing costs prohibitive for some on-board hardwares.

From this point, the FCA technique proposed in [1,12] aims to turn the nonlinear control approach problem presented in (13) into a faster linear version by breaking the problem into two interconnected subsets of VCAs and RCAs. The reasons to choose these rules are:

Preprints (www.preprints.org) | NOT PEER-REVIEWED | Posted: 5 July 2021 doi:10.20944/preprints202107.0081.v1

- The nonlinearities were broken into independent problems and solved recursively and iteratively;
- With a subsystem coupling all others together, the solution speed and solvability was enhanced;
- Although this approach is not robust as Interior Point algorithms, it is fast and well established in the literature [24].

Taking this into account, the QTR CEM was broken into two different problems such as:

$$\hat{\boldsymbol{\tau}}_a = \boldsymbol{M_a}(\boldsymbol{u_b})\boldsymbol{u}'_{\boldsymbol{a}} \tag{15}$$

$$\hat{\boldsymbol{\tau}}_b = \boldsymbol{M_b}(\boldsymbol{u_a})\boldsymbol{u_b} \tag{16}$$

where $\boldsymbol{u_a} \in \mathbb{R}^4$, $\boldsymbol{u}'_a \in \mathbb{R}^5$, $\boldsymbol{u_b} \in \mathbb{R}^4$, $\hat{\boldsymbol{\tau}}_a \in \mathbb{R}^2$, $\hat{\boldsymbol{\tau}}_b \in \mathbb{R}^5$, $\boldsymbol{M_a}(\boldsymbol{u_a}) \in \mathbb{R}^{2\times5}$ and $\boldsymbol{M_b}(\boldsymbol{u_b}) \in \mathbb{R}^{5\times4}$. Also, $\boldsymbol{u_a} \cup \boldsymbol{u_b} = \boldsymbol{u}$ and $\boldsymbol{M_a} \subset \boldsymbol{M_b} \subset \boldsymbol{M}$ [12].

By consequence, these subsystems are shown in (17) and (18):

$$\overbrace{\begin{bmatrix} X^b \\ N^b \end{bmatrix}}^{\hat{\tau}_a} = \overbrace{\begin{bmatrix} k_1\delta_1 & k_1\delta_2 & k_1\delta_3 & k_1\delta_4 & 0 \\ -k_1 d\delta_1 & -k_1 d\delta_2 & k_1 d\delta_3 & k_1 d\delta_4 & k_2(\delta_1 c\gamma_1 + \delta_2 c\gamma_2) - k_2(\delta_3 c\gamma_3 + \delta_4 c\gamma_4) \end{bmatrix}}^{\boldsymbol{M_a}(\boldsymbol{u_b})} \overbrace{\begin{bmatrix} \sin(\gamma_1) \\ \sin(\gamma_2) \\ \sin(\gamma_3) \\ \sin(\gamma_4) \\ 1 \end{bmatrix}}^{\boldsymbol{u}'_a} \tag{17}$$

$$\overbrace{\begin{bmatrix} X^b \\ Z^b \\ L^b \\ M^b \\ N^b \end{bmatrix}}^{\hat{\tau}_b} = \overbrace{\begin{bmatrix} k_1 s\gamma_1, & k_1 s\gamma_2, & k_1 s\gamma_3, & k_1 s\gamma_4 \\ k_1 c\gamma_1, & k_1 c\gamma_2, & k_1 c\gamma_3, & k_1 c\gamma_4 \\ (-k_1 dc\gamma_1 - k_2 s\gamma_1), & (k_1 dc\gamma_2 - k_2 s\gamma_2), & (k_1 dc\gamma_3 + k_2 s\gamma_3), & (-k_1 dc\gamma_4 + k_2 s\gamma_4) \\ k_1 dc\gamma_1, & -k_1 dc\gamma_2, & k_1 dc\gamma_3, & -k_1 dc\gamma_4 \\ (-k_1 ds\gamma_1 + k_2 c\gamma_1), & (k_1 ds\gamma_2 + k_2 c\gamma_2), & (k_1 ds\gamma_3 - k_2 c\gamma_3), & (k_1 ds\gamma_4 - k_2 c\gamma_4) \end{bmatrix}}^{\boldsymbol{M_b}(\boldsymbol{u_a})} \overbrace{\begin{bmatrix} \delta_1 \\ \delta_2 \\ \delta_3 \\ \delta_4 \end{bmatrix}}^{\boldsymbol{u_b}} \tag{18}$$

where $\boldsymbol{u}'_a = [\sin^{-1}(\gamma_1), \sin^{-}(\gamma_2), \sin^{-}(\gamma_3), \sin^{-}(\gamma_4), 1]^T$. To obtain $\boldsymbol{u_a}$, it is necessary to take the first 4 elements of $\boldsymbol{u}'_a$.

It is important to remark that the chosen subsystem combination allows the QTR to perform maneuvers using the motors differential rotation speeds and/or tilting its servomotors independently. It means that the VCAs $[X^b, N^b]^T$ are directly actuated by the RCAs $\boldsymbol{u_a}$. Considering that $[X^b, N^b]^T$ are reached, the remaining VCAs $[Z^b, L^b, M^b]^T$ acts on the RCAs $\boldsymbol{u_b}$.

For feasible constrained solutions, the PMSs and servomotors tilting angle ranges had the normalized values of $[0, 1] = [0, 100\%]$ and $[-1, +1] = [-30, +30]$, respectively.

More details about the control allocation technique are depicted in [1,12].

4. SITL Scheme

The SITL simulator allows you to run the QTR without any hardware device. It is a build of the autopilot code using an ordinary C++ compiler, giving to the user a native executable to test the aircraft in a virtual environment.

For this matter, the experiments were carried out to emulate the computational effort of the FCA, where all the aircraft dynamics and kinematics responses are from SITL simulator. Therefore, the threshold times in the FCA execution directly interfere in the system dynamics due to the respective control loop parallel operation.

To illustrate the procedure, Figure 3 shows the SITL block diagram.

Preprints (www.preprints.org) | NOT PEER-REVIEWED | Posted: 5 July 2021 doi:10.20944/preprints202107.0081.v1

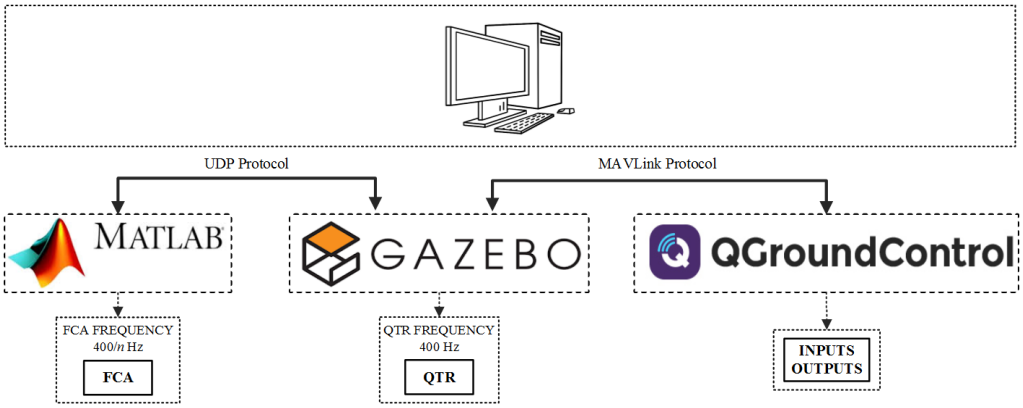

Figure 3. SITL block diagram illustration.

The figure above depicts the software used to run the SITL. The vehicle modelled and presented in Section 2 was inserted inside the Gazebo platform, with all the equipment characteristics. It establishes connection with Matlab via UDP protocol, where the FCA technique runs at $400/n$ Hz of frequency, making it possible to analyze the minimum frequency allowed to run the control allocation technique without destabilizing the QTR. The communication with QGroundControl is established through MAVLink protocol, where the aircraft inputs and outputs can be manipulated, creating a virtual environment.

To complement the SITL illustration, Figure 4 shows the MIMO control loop of the SITL simulation.

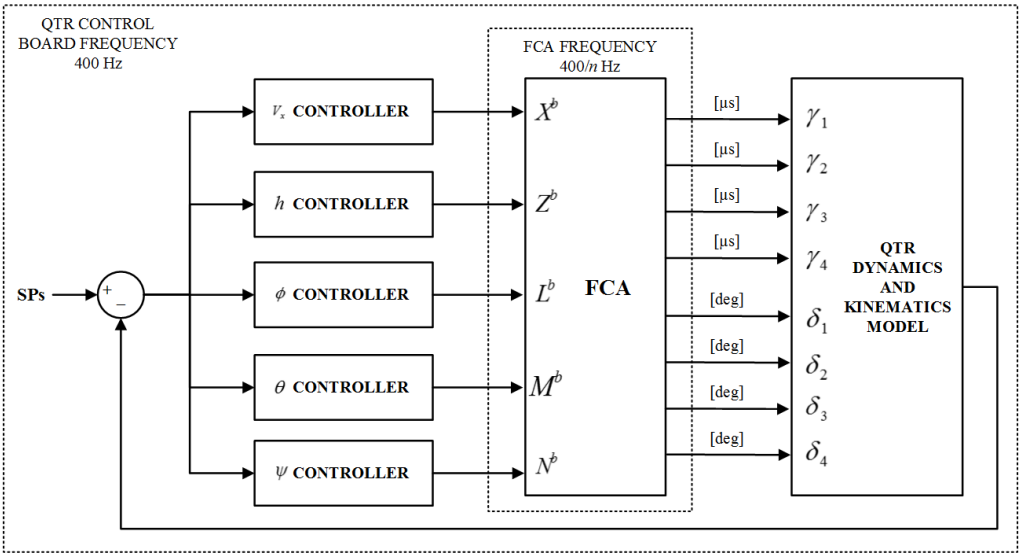

Figure 4. Illustration of the parts that have different sampling frequency.

From the figure above it is possible to see that the FCA technique can have a different frequency from the QTR control board, represented by $400/n$ Hz, where n is the limit number to be obtained for safe and reliable flight conditions.

It should be noted that the 3 critical DoFs for the QTR stability are roll, pitch and altitude [20]. Thus, through the Integral of the Squared Error (ISE) index, a threshold was established to define the vehicle instability/fall, which consequently generates a maximum time/minimum frequency of the FCA operation. These limits are shown in Table 1, obtained through experimental curves flying under similar conditions. Then, if bigger controlled responses are obtained, the delay time at that simulation extrapolated the QTR controllability conditions.

Preprints (www.preprints.org) | NOT PEER-REVIEWED | Posted: 5 July 2021 doi:10.20944/preprints202107.0081.v1

Table 1: Values of the ISE indexes obtained through experimental tests.

DoF	ISE
Roll ($\boldsymbol{\phi}$)	9×10^3
Pitch ($\boldsymbol{\theta}$)	1×10^1
Backward/Forward Velocity ($\boldsymbol{V_x}$)	1×10^1

This index was chosen because a system based on it would have reasonable damping and a satisfactory transient response, punishing errors in the quadratic weights during the experiment, regardless of the time they occur [25,26].

5. Simulation Results

For better understanding and shows analysis the effect of the frequency control allocation variation on the QTR stability, this section is divided into 2 main parts: the first one depicts the DoF controlled responses as the delay time of the control allocation variation is changed; the second one illustrates some three-dimensional results, aiming to obtain the minimum frequency for the control allocation operation.

5.1. Remarks about the Control Technique

Besides, it is not the purpose of this work neither analyze nor demonstrate the controller topology. For this work, it was used the Successive Loop Closure as presented in [27]. However, several other control methodologies could provide similar results [28,29].

5.2. Kinematics and Dynamics Control Results

This section will present some simulation results that aim to analyze the QTR dynamics responses considering 3 different delay times that the FCA technique spent to process the VCAs, demanded by the 5 controllers.

In order to illustrate the controlled responses, Figure 5 and 6 present the vehicle behavior for 3 different delay times of the FCA operation. Randomly, the SetPoints (SPs) were: $h^d = 10$ m at 0 sec, $V_x^d = 3$ m/s at 10 sec, $\phi^d = 0°$, $\theta^d = 0°$ and $\psi^d = 0°$ at 0 sec. Then, the red, black and blue curves represent $n = 1$, 2 and 4, respectively.

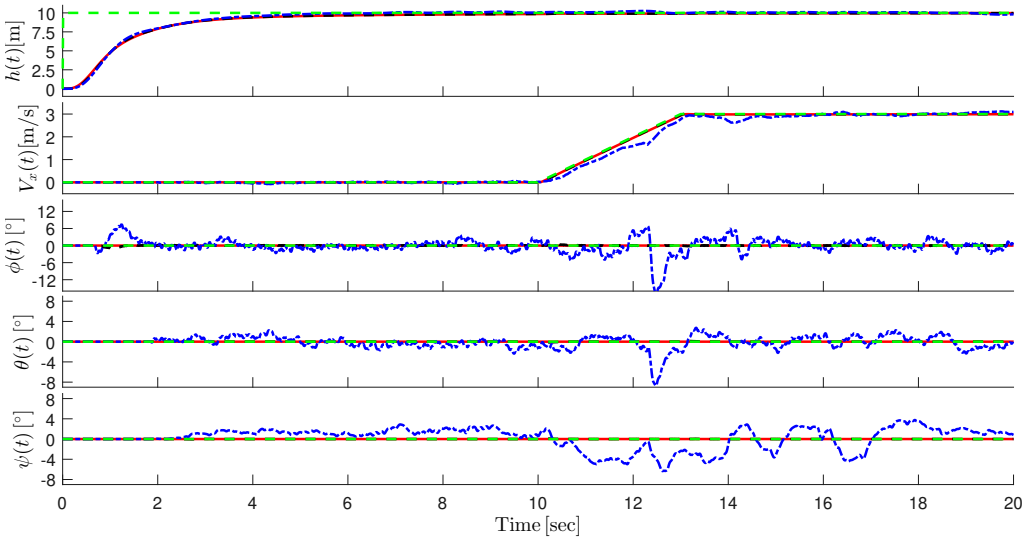

Figure 5. Controlled responses for altitude, forward/backward velocity, rolling, pitching and yawing dynamics.

Preprints (www.preprints.org) | NOT PEER-REVIEWED | Posted: 5 July 2021 doi:10.20944/preprints202107.0081.v1

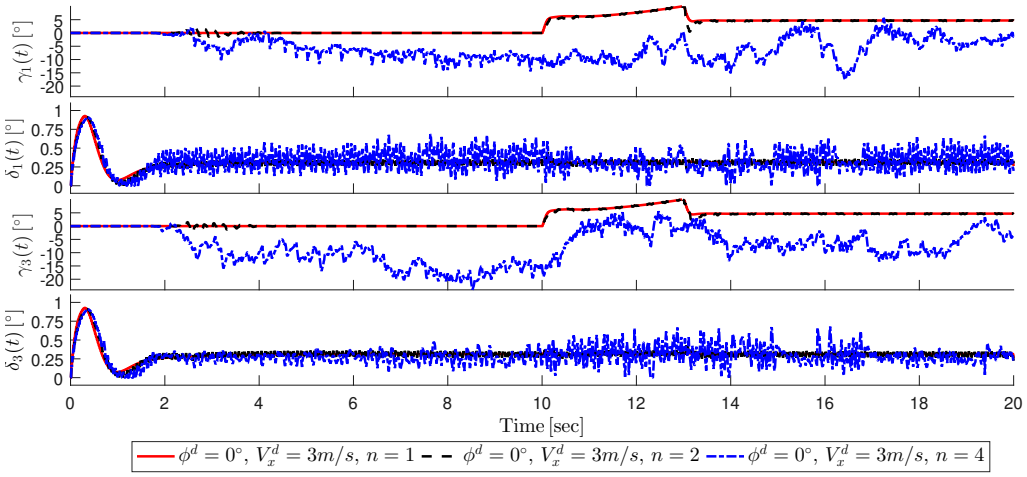

Figure 6. QTR RCAs - Propulsion motors and servomotors numbers 1 and 3.

Figure 5 shows that as the time demanded to process the control allocation increases, the vehicle starts to show oscillatory characteristics around the SPs, because the RCAs do not match to the VCAs required at that instant loop iteration. For this situation, the minimum frequency of a control allocation acceptable operation would be 100 Hz.

Figure 6 illustrates the RCAs of propulsion systems 1 and 3, on the QTR front part, as shown in Figure 1. The RCAs of systems 2 and 4 showed similar responses. Thus, it is noted that as n increases, the RCAs start to show impractical amplitudes and oscillations for open field tests, which leads to the conclusion that, for this presented SPs, if the allocation control task had a frequency 5 times lower than the control board frequency, the vehicle would be unstable or crash to the ground.

5.3. Three-Dimensional Results

This section shows simulation results in three-dimensional graphics for different SPs, close to the SP range considered in the controller tuning, aiming to obtain the minimum frequency for each case. This range was based on the parameters presented by the author in the work [1,12]. In this way, the pitching SP was kept at 0 degrees flying at 10 m altitude. The rolling SP ranged from -10 to 10 degrees and the forward/backward velocity were from -3 to 3 m/s, both requested in 10 seconds of flight after take off.

Figure 7 and 8 show the QTR behavior in a three-dimensional perspective and in a top view, respectively.

Preprints (www.preprints.org) | NOT PEER-REVIEWED | Posted: 5 July 2021 doi:10.20944/preprints202107.0081.v1

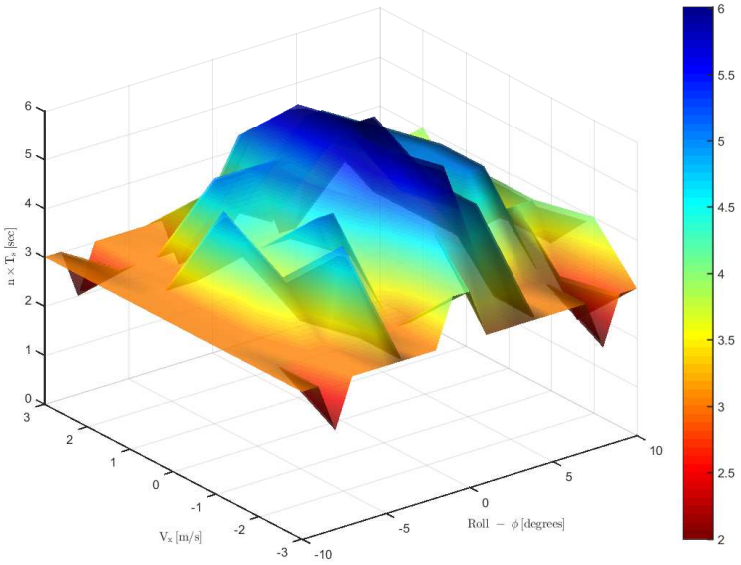

Figure 7. Three-dimensional graph where $400/n$ is the FCA operation frequency.

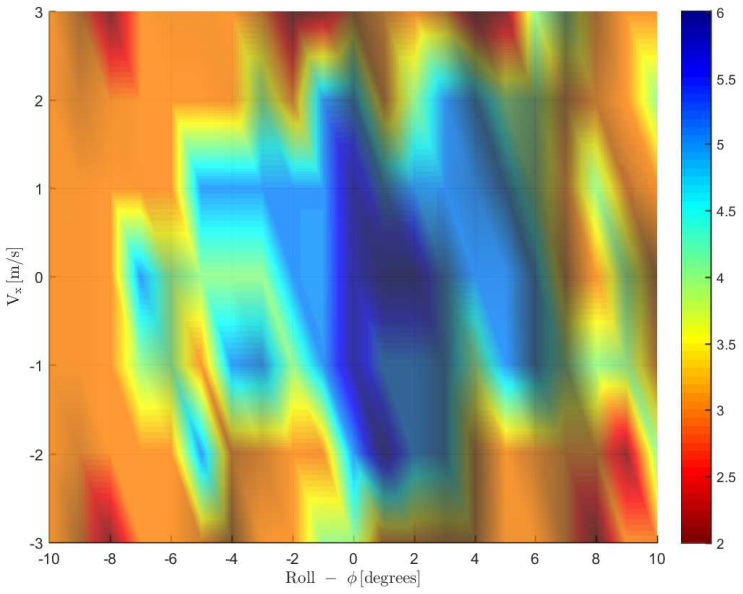

Figure 8. Three-dimensional top view graph.

It should be noted that as the vehicle presents a greater range of roll and forward/reverse velocity, the control allocation technique starts demanding more time to transform the VCAs into RCAs. While a leveled flight allows a control allocation operation with a minimum frequency around 67 Hz (6 times lower than that of the system used, $400H$), the extreme points of the considered ranges do not allow values lower than 200 Hz (2 times lower). It can be concluded that the control allocation technique should not be performed with frequencies of less than 200 Hz for flights within the control requirements considered in [1,12].

Discontinuities between some operating points in their respective neighborhoods can be explained by the vehicle model nonlinearities. In addition, the insertion of

Gaussian noises in the control loops means that the proximity of each operation point can not have a unique solution.

6. Conclusions

This work can be summarized into 2 stages: Design and control of an over-actuated UAV; Development of the SITL simulation considering different delay times for FCA technique operation; Performance of simulation tests.

For the first step, it is possible to conclude that the QTR vehicle was modeled in controlled satisfactorily considered that the FCA technique has the same frequency of the control board, 400 Hz. Therefore, it was a crucial step for the FCA development and implementation.

The principal and more important step in this work is the SITL simulation, which allowed to obtain the minimum frequency acceptable for the control allocation execution: 200 Hz. Lower frequencies than this one would cause instability or crashes in the QTR operation.

As future works, test bench and open field flights are now able to be performed, aiming to validate the simulation tests.

Data Availability Statement: The authors declare that there are no external data and materials.

Acknowledgments: The authors thank CEFET-MG, UFJF, TBE and Leuphana University of Lüneburg for the financial support.

Conflicts of Interest: The authors declare that they have no conflict of interest.

References

1. Santos, M.F. Alocação de Controle Desacoplada Rápida em Sistemas de Controle Superatuados. PhD thesis, UFJF, 2019.
2. Ferreira, F.C.; Santos, M.F.; Schettino, V.B. Computational vision applied to mobile robotics with position control and trajectory planning: Study and application. 19th International Carpathian Control Conference (ICCC). IEEE, 2018.
3. Silva, M.F.; Cerqueira, A.S.; Vidal, V.F.; Honório, L.M.; Santos, M.F.; Oliveira, E.J. Landing area recognition by image applied to an autonomous control landing of VTOL aircraft. 18th International Carpathian Control Conference (ICCC). IEEE, 2017, pp. 240–245.
4. Prisco, G.M.; Rosa, D.J. Methods for handling an operator command exceeding a medical device state limitation in a medical robotic system, 2017. US Patent 9,566,124.
5. Santos, M.F.; Pereira, V.S.; Ribeiro, A.C.; Silva, M.F.; Carmo, M.J.; Vidal, V.F.; Honório, L.M.; Cerqueira, A.S.; Oliveira, E.J. Simulation and comparison between a linear and nonlinear technique applied to altitude control in quadcopters. 18th International Carpathian Control Conference (ICCC). IEEE, 2017, pp. 234–239.
6. Liu, Y.; Wang, Q.; Hu, H.; He, Y. A novel real-time moving target tracking and path planning system for a quadrotor UAV in unknown unstructured outdoor scenes. *IEEE Transactions on Systems, Man, and Cybernetics: Systems* **2018**, pp. 1–11.
7. Minaeian, S.; Liu, J.; Son, Y.J. Vision-based target detection and localization via a team of cooperative UAV and UGVs. *IEEE Transactions on systems, man, and cybernetics: systems* **2016**, *46*, 1005–1016.
8. Klausen, K.; Fossen, T.I.; Johansen, T.A. Autonomous recovery of a fixed-wing UAV using a net suspended by two multirotor UAVs. *Journal of Field Robotics* **2018**, *35*, 717–731.
9. Warren, M.; Mejias, L.; Kok, J.; Yang, X.; Gonzalez, F.; Upcroft, B. An Automated Emergency Landing System for Fixed-Wing Aircraft: Planning and Control. *Journal of Field Robotics* **2015**, *32*, 1114–1140.
10. Johansen, T.A.; Fossen, T.I. Control allocation - A survey. *Automatica* **2013**, *49*, 1087–1103.
11. Saied, M.; Shraim, H.; Lussier, B.; Fantoni, I.; Francis, C. Local controllability and attitude stabilization of multirotor UAVs: Validation on a coaxial octorotor. *Robotics and Autonomous Systems* **2017**, *91*, 128–138.
12. Santos, M.F.; Honório, L.M.; Moreira, A.P.G.M.; Silva, M.F.; Vidal, V.F. Fast Real-Time Control Allocation Applied to Over-Actuated Quadrotor Tilt-Rotor. *Journal of Intelligent & Robotic Systems* **2021**, *102*, 1–20.
13. Gai, W.; Liu, J.; Zhang, J.; Li, Y. A New Closed-loop Control Allocation Method with Application to Direct Force Control. *International Journal of Control, Automation and Systems* **2018**, *16*, 1355–1366.
14. Durham, W.C. Constrained control allocation. *Journal of Guidance, Control, and Dynamics* **1993**, *16*, 717–725.
15. Ahani, A.; Ketabdari, M.J. Alternative approach for dynamic-positioning thrust allocation using linear pseudo-inverse model. *Applied Ocean Research* **2019**, *90*, 101854.
16. Shi, J.; Zhang, W.; Li, G.; Liu, X. Research on allocation efficiency of the redistributed pseudo inverse algorithm. *Science China Information Sciences* **2010**, *53*, 271–277.
17. Bodson, M.; Frost, S.A. Load balancing in control allocation. *Journal of Guidance, Control, and Dynamics* **2011**, *34*, 380–387.

18. Simon, D.; Härkegård, O.; Löfberg, J. Command governor approach to maneuver limiting in fighter aircraft. *Journal of Guidance, Control, and Dynamics* **2016**, *40*, 1514–1527.
19. Oliveira, E.J.; Oliveira, L.W.; Pereira, J.L.R.; Honório, L.M.; Junior, I.C.S.; Marcato, A.L.M. An optimal power flow based on safety barrier interior point method. *International Journal of Electrical Power & Energy Systems* **2015**, *64*, 977–985.
20. Beard, R.W.; McLain, T.W. *Small unmanned aircraft: Theory and practice*; Princeton University Press: Princeton, EUA, 2012.
21. Fossen, T.I. Mathematical models for control of aircraft and satellites. *Department of Engineering Cybernetics Norwegian University of Science and Technology* **2011**.
22. Burggräf, P.; Martínez, A.R.P.; Roth, H.; Wagner, J. Quadrotors in factory applications: design and implementation of the quadrotors P-PID cascade control system. *SN Applied Sciences* **2019**, *1*, 722.
23. de Souza, A.C.Z.; Honório, L.d.M.; Torres, G.L.; Lambert-Torres, G. Increasing the loadability of power systems through optimal-local-control actions. *IEEE Transactions on Power Systems* **2004**, *19*, 188–194.
24. Dennis Jr, J.E.; Schnabel, R.B. *Numerical methods for unconstrained optimization and nonlinear equations*; Vol. 16, Siam, 1996.
25. dos Santos, M.F. Controle Tolerante a Falhas de um Sistema de Propulsão de Hexacópteros. Master's thesis, UFJF, 2014.
26. Shahemabadi, A.R.; Noor, S.B.M.; Taip, F.S. Analytical formulation of the integral square error for linear stable feedback control system. *International Conference on Control System, Computing and Engineering* **2013**, pp. 157–161.
27. Beard, R.W.; McLain, T.W. *Small unmanned aircraft: Theory and practice*; Princeton university press, 2012.
28. Argentim, L.M.; Rezende, W.C.; Santos, P.E.; Aguiar, R.A. PID, LQR and LQR-PID on a quadcopter platform. International Conference on Informatics, Electronics and Vision (ICIEV). IEEE, 2013, pp. 1–6.
29. Zhao, W.; Go, T.H. Quadcopter formation flight control combining MPC and robust feedback linearization. *Journal of the Franklin Institute* **2014**, *351*, 1335–1355.